IJMT. Vol. 22, Iss. 2, 2026. (29-47)

International Journal of Maritime Technology

Journal homepage: ijmt.ir

Optimizing Hydrophone Array Configurations for 6-DOF Motion-Induced Phase Error Correction in Synthetic Aperture Sonar Imaging

Hamid Hajirahimi Kashani[1*], Seyed Alireza Seyedin[2]

[1] *PhD. student, Faculty of Engineering, Ferdowsi University of Mashhad, Mashhad, Iran; hajirahimi.hamid@mail.um.ac.ir*
[2] *Professor, Faculty of Engineering, Ferdowsi University of Mashhad, Mashhad, Iran; seyedin@um.ac.ir*

ARTICLE INFO

Article History:
Received: 12 Aug 2025
Last modification: 16 Apr 2026
Accepted: 18 Apr 2026
Available online: 21 Apr 2026

Article type:
Research paper

Keywords:
Synthetic Aperture Sonar (SAS);
6-DoF motion;
Phase Sensitivity Index (PSI);
Hydrophone Array Optimization;
Back-Projection

ABSTRACT

Synthetic aperture sonar (SAS) achieves high-resolution imaging by coherently integrating echoes along the platform trajectory, making it inherently sensitive to six-degree-of-freedom (6-DOF) motion. Sub-wavelength perturbations distort phase, broaden the main lobe, and raise sidelobes. This paper introduces a geometry-centric array optimization framework that: (i) operationalizes a Phase Sensitivity Index (PSI) with translational and rotational components to quantify array-dependent motion sensitivity; and (ii) calibrates PSLR/ISLR to image signatures (main-lobe width and sidelobe proximity) against a back-projection (BP) reference, ensuring physics-consistent visual interpretation. Three receiver arrays—2D planar, 3D cubic, and 3D hemispherical (36 elements each)—are evaluated under six motions (surge, sway, heave, roll, pitch, yaw) and three imaging states (ideal, motion-degraded, corrected), yielding 54 scenarios. Motion parameters reflect realistic autonomous underwater vehicle conditions: translational RMS 2.0–3.2 mm, rotational RMS 0.25°–0.35°, platform speed 2.5 m/s, and dominant 0.2–2 Hz content. The hemispherical array attains the lowest normalized PSI and consistently superior sidelobe metrics, outperforming the planar array by approximately 6.5 dB in PSLR and 5.6 dB in ISLR on updated corrected global means, and the cubic array by approximately 2.9 dB in both PSLR and ISLR. Yaw and Heave cause the greatest degradation; Roll is least harmful. Motion correction improves PSLR by ≥4 dB and ISLR by ≥3 dB relative to degraded images, while the residual gap to ideal remains ≤4 dB, by design. The proposed framework enables quantitative array selection and supports robust SAS imaging in embedded AUVs without external navigation sensors.

ISSN: 2645-8136

DOI:

1. Introduction

Synthetic aperture sonar (SAS) achieves high cross-range resolution by coherently integrating echoes along the platform trajectory; this coherence, however, makes image quality acutely sensitive to six-degree-of-freedom (6-DOF) motion. Sub-wavelength perturbations in translation (surge, sway, heave) and rotation (roll, pitch, yaw) induce path-length and time-delay errors that broaden the main lobe and elevate sidelobes, degrading interpretability and downstream detection/classification performance. In practice, platform dynamics, low signal-to-noise ratio (SNR), and bandwidth–angle coupling in wide-swath, multi-receiver configurations aggravate these effects and challenge purely post-processing remedies [1].

1.1. Motion Models and Scenario Matrix

Classical mitigation follows two main routes. The first is sensor-aided motion compensation (MOCO), in which navigation data (e.g., INS/DVL) are fused and applied within range–Doppler or ω–k pipelines. The staging of range-independent versus range-dependent compensation is critical, and in high-resolution regimes, one-step MOCO (moving range-dependent terms before range-cell migration correction) is preferred to avoid RCMC mismatch and residual migration artifacts [2]. The second route is echo-based autofocus, including sub-aperture and space-variant formulations tailored to multi-receiver, wide-beam SAS, which estimate residual phase directly from the data and compensate yaw-/squint-driven, range-dependent errors prior to final focusing [3].
Even with sophisticated MOCO and autofocus, non-negligible residual phase errors often persist, especially when motion is anisotropic and the phase center varies across receivers. This observation motivates a complementary, design-time lever: selecting the receiver array geometry so that motion-induced phase sensitivity is intrinsically damped before any post-processing is applied. In this work we treat array geometry as a primary design variable, on par with waveform and processing, and investigate how alternative layouts change the way 6-DOF motion is "seen" by the phase history and by image-domain sidelobe metrics.

1.2. Related Work

Recent advances in multi-receiver SAS imaging further illuminate where phase residuals arise and how algorithmic structure interacts with hardware geometry. Specifically, the spatial distribution of receivers dictates the spatial sampling rate of the synthetic aperture, which in turn influences the coherence of the backprojected signals. When motion-induced phase errors are present, the geometric diversity of the array determines the robustness of the reconstruction process against micro-motion decorrelation. Consequently, optimizing the element arrangement moving beyond traditional planar configurations to more complex 3D geometries provide a physical layer of mitigation that complements sophisticated motion-compensation algorithms.

1.2.1. MOCO/Autofocus Methods

Frequency-domain families based on extended chirp scaling account for higher-order range–azimuth coupling and residual quadratic terms that grow off the reference range; sub-block and range-blocking strategies reduce space variance and improve focusing on simulations and real data [4]. Low-rank and generalized PCA formulations recast multi-receiver SAS into a model amenable to joint motion/scene parameter estimation in a reduced subspace, enabling robust imaging under practical conditions [5].
Complementarily, two-stage sub-aperture MOCO for wide-beam, multi-receiver SAS first compensates a beam-center term per hydrophone and then corrects the residual space-variant term in the range–Doppler domain, yielding tangible gains in sidelobe metrics and focus [3]. Collectively, these works demonstrate that careful integration of navigation sensors, frequency-domain focusing, and autofocus can substantially reduce motion-induced blurring and sidelobe growth. However, they also indicate that residual phase errors remain, particularly under complex trajectories and wide apertures, and that performance can depend subtly on the underlying array geometry.

1.2.2. Array-Geometry Design and Robustness Metrics

In parallel with algorithmic progress, a substantial body of work has examined how array geometry influences robustness and sidelobe behavior. Hydrophone array design studies often adopt a "shape-before-placement" methodology: candidate shapes are ranked by the stability of maximum sidelobe level (MSL) across frequency, and then sensor positions are optimized within the chosen shape to maintain low sidelobes without sacrificing resolution; sea trials confirm that compact, axisymmetric three-dimensional (3D) shapes can preserve sidelobe floors under practical constraints [6]. Related evidence from circular and volumetric SAS imaging on surface or unmanned surface vehicles (USVs) demonstrates how non-linear array and trajectory geometries can regularize conical sidelobes and enable 3D reconstruction with calibrated processing chains [1].
Broader array-processing literature likewise links geometry and spatial sampling to robustness. Fibonacci-patterned apertures for broadband acoustic cameras, for example, report reduced grating lobes and improved focusing compared to regular grids [7], while classical array design in the DOA/IET canon emphasizes the role of aperture layout in controlling aliasing, mutual coupling, and estimator stability [8].

Beyond SAS, studies on spatial aliasing in microphone and sonar arrays quantify how geometry and motion jointly determine the usable spatial bandwidth, reinforcing that sidelobe and aliasing control is a first-order design variable not merely a signal-processing afterthought [8,9].

These findings suggest that compact, axisymmetric 3D layouts such as hemispherical arrays may offer improved robustness over planar or cubic arrays under realistic motion, by distributing baselines in 3D and regularizing angular sampling. However, a systematic, quantitative comparison of such geometries under 6-DOF motion, using metrics tied directly to SAS image quality, remains limited.

1.3. Novel Contributions and Paper Organization

This paper addresses the above gap by proposing a geometry-centric framework for optimizing hydrophone receiver arrays in multi-receiver SAS under realistic 6-DOF motion. We operationalize the geometry lever using two complementary metric families:

- A normalized Phase Sensitivity Index (PSI), with separate translational and rotational components, extracted from perturbed phase histories to quantify how array geometry amplifies or attenuates motion-induced phase errors; and
- Image-domain Peak Sidelobe Ratio (PSLR) and Integrated Sidelobe Ratio (ISLR), computed from back-projection (BP) reconstructions to characterize main-lobe width and sidelobe proximity.

A calibrated BP reference ties PSI to PSLR/ISLR through a metric-to-image mapping, so that changes in PSI correspond to interpretable image signatures. Using a controlled pipeline, we evaluate three 36-element receiver arrays 2D planar, 3D cubic, and 3D hemispherical under six elementary motions (surge, sway, heave, roll, pitch, yaw) and three imaging states (ideal, motion-degraded, motion-corrected), totaling 54 scenarios. The processing chain (MOCO and imaging) is held fixed across arrays to isolate geometry, while motion statistics reflect realistic AUV conditions.

The main contributions of this work are as follows:

- A normalized Phase Sensitivity Index (PSI) is introduced, tailored to multi-receiver SAS and decomposed into translational and rotational components, demonstrating how it can be used to rank array geometries in terms of motion-induced phase sensitivity.
- The PSI is calibrated against BP-based PSLR/ISLR metrics, enabling direct interpretation of PSI changes in terms of image-domain main-lobe broadening and sidelobe behavior.
- A systematic comparison is performed across planar, cubic, and hemispherical 36-element arrays under 54 motion scenarios, revealing that hemispherical layouts can deliver approximately 6.5 dB improvement in PSLR and 5.6 dB improvement in ISLR over planar arrays on updated corrected global means, while also retaining an advantage of approximately 2.9 dB in both PSLR and ISLR over cubic arrays under identical motion statistics. In this work we augment the PSI definition with the additional terms described in the next section.

These results provide quantitative, geometry-based guidance for array selection in embedded AUV SAS systems, and illustrate how design-time choices in array geometry can complement sensor-aided MOCO and autofocus. The remainder of the paper is organized as follows. Section 2 presents the problem formulation and methodology, including the system model, motion scenarios, PSI definition, and image-quality metrics. Section 3 describes the system and waveform specification as well as the simulation and processing setup. Section 4 details the targets, evaluation metrics, and the figure-generation protocol used for reporting. Section 5 reports and discusses the PSI and PSLR/ISLR results across all geometries and motion components. Section 6 concludes the paper, and Section 7 outlines directions for future work.

2. Problem Formulation and Methodology

We consider a monostatic synthetic aperture sonar (SAS) with a receiving hydrophone array mounted on a moving platform. Let $r_p(t) \in R^3$ denote the platform reference point, $R(t) \in \mathrm{SO}(3)$ the rotation matrix (roll–pitch–yaw), and $r_n \in R^3$ the position of the n_{th} hydrophone in the body frame. A point target at $x \in R^3$ generates a baseband return at element n:

$$s_n(t) = a(x)\exp\left\{-j\,\frac{4\pi}{\lambda}\left\|x-(r_p(t)+R(t)r_n)\right\|\right\} \quad (1)$$
$$+\eta_n(t)$$

where λ is the acoustic wavelength, a(x) encodes target reflectivity and propagation loss, and $\eta_n(t)$ is noise, $r_p(t)$ is platform trajectory; R(t) is rotation and r_n is hydrophone position.

Under small 6-DOF perturbations, $r_p(t) = \overline{r_p}(t) + \delta r(t)$ and $R(t) \approx I + \Omega(t)$. Here $I \in R^3$ denotes the 3×3 identity matrix. and Ω(t) is skew-symmetric and represents the infinitesimal rotation vector $\delta\theta(t) = [\phi, \theta, \psi]^T$ via $\Omega(t)v = \delta\theta(t) \times v$ Evaluate the unit line-of-sight (LOS) vector on the nominal path:

$$\hat{u}_n(t;x) = \frac{x-(\bar{r}_p(t)+r_n)}{\left\|x-(\bar{r}_p(t)+r_n)\right\|} \quad (2)$$

Linearizing the phase at $k_0 = 2\pi/\lambda$ yields:

$$\Delta\varphi_n(t;x) \approx k_0\hat{u}_n^T\,\delta r(t) + k_0\hat{u}_n^T(t;x)\Omega(t)r_n \quad (3)$$

and, equivalently, using $\Omega r_n = \delta\theta \times r_n$

$$\Delta\varphi_n(t;x) \approx k_0\hat{u}_n^{\cdot}\,\delta r(t) + k_0(\hat{u}_n(t;x)\times r_n)^{\cdot}\,\delta\theta(t) \quad (4)$$

Where δr(t) is translational jitter (surge, sway, heave), $\delta\theta(t)$ is infinitesimal rotation (roll, pitch, yaw), $\hat{u}_n$ is LOS unit vector on the nominal path and $k_0 = 2\pi/\lambda$.

2.1. Phase Sensitivity Index (PSI)

For motion component $\xi \in \{6-\text{DoF}\}$ define the phase Jacobian $J_{n,\xi}(t;x) = \frac{\partial\Delta\varphi_n(t;x)}{\partial\xi}$. Aggregating over N elements and coherent aperture Γ gives:

$$PSI_\xi \propto \frac{1}{NT}\int_\Gamma \sum_{n=1}^{N}\left|J_{n,\xi}(t;x_0)\right|^2 dt \quad (5)$$

Where $T = |\Gamma|$ and evaluated at a representative focus point x_0. We normalize to compare across arrays and apertures:

$$PSI_\xi \propto \frac{PSI_\xi}{(\frac{4\Pi}{\lambda})^2 L^2} \quad (6)$$

where L is a characteristic aperture scale (e.g., effective radius), N is number of hydrophones in the array that essentially quantifying the array's size, Γ is coherent processing interval, $J_{n,\xi}$ is phase Jacobian, L is geometry scale. Smaller PSI_ξ indicates a phase-quiet geometry with regard to motion ξ.

$$PSI = \frac{1}{2N}\sum_{i=1}^{N}\frac{(\Delta\phi_i)^2}{\sigma_{motion}^2} \quad (7)$$

$\Delta\emptyset_i$ denotes the total phase shift experienced by the i-th sensor, encompassing all disturbances (motion, mutual-coupling, manufacturing tolerance and multipath) and is expressed in radians; and σ_{motion} is the root-mean-square (RMS) phase variance induced by platform motion, also measured in radians, and serves as the baseline noise level against which phase errors are compared. A larger PSI indicates higher resolution capability but also higher vulnerability to errors. A larger PSI indicates higher resolution capability but also higher vulnerability to errors. If every hydrophone's phase deviates by σ_{motion}, PSI = 1. Larger deviations raise PSI; smaller deviations lower it. PSI is the single quantity that links all physical disturbances to the quality metrics.

2.1.1. Sensitivity of the Proposed PSI Framework

For the n-th hydrophone, let the total residual phase error be written as:

$$\Delta\phi_n^{tot}(t;x) = \Delta\phi_n^{mot}(t;x) + \Delta\phi_n^{coup}(t) + \Delta\phi_n^{tol}(t) + \Delta\phi_n^{mp}(t;x) \quad (8)$$

where

- $\Delta\phi_n^{\text{tot}}(t;x)$ is the Total phase error at hydrophone n,
- $\Delta\phi_n^{\text{mot}}(t;x)$ is the motion-induced phase perturbation already defined by the first-order model,
- $\Delta\phi_n^{\text{coup}}(t)$ is the phase perturbation caused by inter-element mutual coupling,
- $\Delta\phi_n^{\text{tol}}(t)$ is the phase perturbation caused by hydrophone position errors,
- $\Delta\phi_n^{\text{mp}}(t;x)$ is the phase perturbation induced by coherent reflected paths.

The corresponding effective normalized PSI for motion component ξ and geometry $g \in$ {planar, cubic, hemispherical} is defined as

$$PSI_{\xi,g}^{eff} = \frac{4\lambda^2}{L_g^2}\times \frac{1}{NT}\sum_{n=1}^{N}\int_\Gamma \left|\begin{matrix}J_{n,\xi}^{mot}(t;x_0)+J_{n,g}^{coup}(t)\\ +J_{n,g}^{tol}(t)+J_{n,g}^{mp}(t;x_0)\end{matrix}\right|^2 dt \quad (9)$$

where

- λ is the acoustic wavelength,
- L_g is the characteristic aperture scale for geometry g,
- N is the number of hydrophones,
- Γ is the coherent processing interval,
- $T = |\Gamma|$ is the duration of the coherent processing interval,
- x_0 is the representative focus point used for PSI evaluation,
- $J_{n,\xi}^{\text{mot}} = \partial\Delta\phi_n^{\text{mot}}/\partial\xi$,
- $J_{n,g}^{\text{coup}}$, $J_{n,g}^{\text{tol}}$, and $J_{n,g}^{\text{mp}}$ are effective first-order phase-sensitivity terms associated with coupling, tolerance, and multipath, respectively.

For weak non-idealities and approximately uncorrelated perturbation sources, Eq. (9) can be linearized in variance form as:

$$PSI_{\xi,g}^{eff} \approx PSI_{\xi,g}(1+\eta_g^{coup}+\eta_g^{tol}+\eta_g^{mp}) \quad (10)$$

$$\eta_g^q = \frac{\delta_{\phi,g,q}^2}{\delta_{\phi,\xi,,mot,g}^2}, q \in \{coup, tol, mp\} \quad (11)$$

where $\sigma_{\phi,\xi,\text{mot},g}^2$ denotes the motion-induced phase variance for DoF ξ and geometry g, and $\sigma_{\phi,g,q}^2$ denotes the additional phase variance introduced by non-ideality q.

2.1.2. Mutual Coupling

A first-order receive-side coupling model is written as:

$$s_{meas}(t) = C_g S_{ideal}(t), C_g = I + J_g \quad (12)$$

where

- $s_{ideal}(t)$ is the uncoupled complex receive vector,
- $s_{meas}(t)$ is the measured receive vector after coupling,
- I is the identity matrix,
- J_g is the geometry-dependent coupling matrix,
- the off-diagonal terms of J_g represent inter-element leakage.

For weak coupling, the phase perturbation at sensor n can be approximated by:

$$\Delta\phi_n^{coup}(t) = \mathrm{Im}\left\{\sum_{\substack{m=1 \\ m\neq n}}^{N} J_{g,nm} e^{\phi_m(t)-\phi_n(t)}\right\} \quad (13)$$

where

- $J_{g,nm}$ is the (n, m)-th element of the coupling matrix,
- $\phi_n(t)$ is the nominal phase at hydrophone n,
- Im $\{\cdot\}$ denotes the imaginary part.

This term increases the effective phase-noise floor and is generally stronger when the packaging is compact and three-dimensional. In practice, the exact magnitude depends on mechanical layout, baffle design, operating frequency, and mounting constraints. However, under equal aperture and equal element count, it is more reasonable to interpret coupling as an absolute-metric penalty than as an immediate mechanism for overturning the original motion-driven ranking.

2.1.3. Manufacturing Tolerances

Let the actual sensor location be:

$$\Delta\phi_n^{tol}(t) = k_0 \hat{u}_n^{\mathrm{T}}(t; x_0)\delta r_n, k_0 = \frac{2\pi}{\lambda} \quad (14)$$

where

- k_0 is the acoustic wavenumber,
- $\hat{u}_n(t; x_0)$ is the unit line-of-sight vector from sensor $n$to the focus point x_0.

If $\delta r_n$is modeled as a zero-mean random vector with covariance matrix $\Sigma_{r,g}$, then the corresponding phase variance is:

$$\delta_{\phi,g,tol}^2 = k_0^2 \hat{u}^{\mathrm{T}} \sum_{r,g} \hat{u} \approx k_0^2 \delta_{pos,g}^2 \quad (15)$$

where

- $\Sigma_{r,g}$ is the covariance matrix of position errors for geometry g,
- $\sigma_{pos,g}$ is the RMS assembly tolerance.

This contribution acts as an additive phase-noise floor. Its main effect is to shift the absolute PSI upward. It changes the relative ranking only when the geometry-to-geometry PSI margin is comparable to the tolerance-induced phase variance.

2.1.4. Multipath Propagation

For the n-th hydrophone, let the received signal be modeled as a coherent sum of one direct path and K reflected paths:

$$S_n(t) = S_{n,dir}(t) + \sum_{k=1}^{K} a_{k,n} S_{n,ref,k}(t) \times e^{-j\omega\Delta\tau_{k,n}} \quad (16)$$

where

- $s_{n,dir}(t)$ is the direct-path signal,
- $s_{n,ref,k}(t)$ is the k-th reflected component,
- $a_{k,n}$ is the reflection amplitude ratio for path k,
- $\Delta\tau_{k,n}$ is the excess delay of reflected path k,
- $\omega = 2\pi f$ is the angular frequency,
- f is the operating acoustic frequency.

For weak reflections, an effective multipath phase variance may be approximated as

$$\delta_{\phi,g,mp}^2 = \sum_{K=1}^{K} \gamma_{k,g}^2 \Delta\phi_{k,g}^2, \gamma_{k,g} = \frac{P_{k,ref,g}}{P_{dir,g}} \quad (17)$$

where

- $P_{k,ref,g}$ is the power of reflected path $k$for geometry g,
- $P_{dir,g}$ is the direct-path power,
- $\gamma_{k,g}$ is the reflected-to-direct power ratio,

- $\Delta\phi_{k,g}$ is the phase offset associated with the reflected path.

Unlike mutual coupling and tolerance errors, multipath not only perturbs sensor phases but may also bias the empirical mapping between PSI and PSLR/ISLR by injecting structured sidelobe energy and non-local interference. This is particularly relevant because the original manuscript calibrates the PSI-to-image relationship over a bounded normalized-PSI range and does not claim indefinite extrapolation beyond that regime.

2.1.5. Local Impact on the PSI-to-PSLR/ISLR Mapping

Because the original manuscript already establishes a calibrated OLS-based linear mapping between normalized PSI and PSLR/ISLR, the present sensitivity analysis does not introduce a new global regression. Instead, the existing mapping is used locally around the motion-only operating point:

$$\Delta PSLR_{\xi,g}^{ni} \approx a_{\xi}(PSI_{\xi,g}^{eff} - PSI_{\xi,g}) \tag{18}$$

$$\Delta ISLR_{\xi,g}^{ni} \approx b_{\xi}(PSI_{\xi,g}^{eff} - PSI_{\xi,g}) \tag{19}$$

where

- a_{ξ} is the local slope of the calibrated PSI-to-PSLR mapping for motion component ξ,
- b_{ξ} is the local slope of the calibrated PSI-to-ISLR mapping for motion component ξ,
- $\Delta\mathrm{PSLR}_{\xi,g}^{\mathrm{ni}}$ and $\Delta\mathrm{ISLR}_{\xi,g}^{\mathrm{ni}}$ are the estimated penalties caused by the omitted non-idealities.

This treatment is consistent with the manuscript's original calibration procedure, in which regression coefficients are estimated once over the calibration set and then reused for cross-geometry comparison.

2.2. Linking Array Metrics to Image Quality

Let I(x) be a BP reference image:

$$I(x) = \int_{\Gamma} \sum_{n=1}^{N} w(t) s_n(t) \exp \left\{ + j \times \frac{4\pi}{\lambda} \left\| x - (r_p(t) + R(t) r_n) \right\| \right\} dt \tag{20}$$

with apodization w(t). Define PSLR/ISLR via standard main-lobe M and sidelobe S regions:

$$PSLR = 20 \log_{10} \left(\frac{\max_{x \in S} |I(x)|}{\max_{x \in M} |I(x)|} \right) \tag{21}$$

$$ISLR = 10 \log_{10} \left(\frac{\int_S |I(x)|^2 dx}{\int_M |I(x)|^2 dx} \right) \tag{22}$$

2.3. Array Geometries and Aperture Constraints

Three receiver layouts are realized with a fixed element count N=36 and comparable outer-aperture extents: (i) Planar (2D grid within a disk of radius $R_{\perp}$), (ii) Cubic (3D lattice within a cube of side 2R), and (iii) Hemispherical (3D cap of radius R and cap angle θ_{max}). Hemispherical placements use near-uniform spherical coding to reduce clustering. To mitigate spatial aliasing at the highest effective frequency, the minimum spacing satisfies $d_{min} \leq \frac{\lambda_{min}}{2}$.

We compare three 36-element layouts: Planar 2D, Cubic 3D, and Hemispherical 3D. Let $A = \{r_n\}_{n=1}^{36}$ be the set of element positions. Planar arrays place on a uniform grid in a plane; cubic arrays populate a regular 3D lattice; hemispherical arrays place r_n on a spherical cap of radius R using near-uniform spherical codes or low-discrepancy patterns to reduce clustering and coupling. For the hemispherical cap, with spherical angles (θ_n, φ_n) and radius R,

$$r_n^{(Hemi)} = R\left[\sin\theta_n \cos\phi_n, \sin\theta_n \sin\phi_n, \cos\theta_n\right]^{\cdot} \tag{23}$$

$$\theta_n \in [0, \theta_{\max}], \phi_n \in [0, 2\pi]$$

Axisymmetric and 3D baseline distribution in (23) reduce the average magnitude of the Jacobians $J_{n,\xi}$, hence lower $\widehat{PSI_{\xi}}$ than planar/cubic layouts at identical N and aperture, consistent with sidelobe resolution trade-offs in array design [6–9].

2.4. Imaging and Motion-Correction Settings

All arrays share the same processing backbone: pulse compression, coherent summation, and BP (Eq. 20). Three imaging states are considered: (i) Ideal: $\delta r(t) = 0, \delta\theta(t) = 0$; (ii) Motion-Degraded: Realistic AUV perturbations—translational RMS 2−3.22 mm, rotational RMS 0.25°−0.35°, platform speed 2.5 m/s, dominant motion 0.2−2 Hz—applied one DOF at a time. (iii) Corrected: standard MOCO/autofocus (subaperture, space-variant as needed) prior to BP, following recent multireceiver two-stage subaperture strategies and wideband frequency-domain focusing [3–5].

We sweep six motions (surge, sway, heave, roll, pitch, yaw). For each (array, motion, state) we compute $\widehat{PSI_{\xi}}$ and {PSLR, ISLR}. The design spans 54 scenarios (3 arrays × 6 DOFs × 3 states), consistent with best practices for space variance and wide-beam effects in multireceiver SAS and with one-step MOCO placement that improves RCMC consistency in high-resolution regimes [2].

Positioning relative to prior work Sensor-aided MOCO and echo-based autofocus remain essential for squint and space-variant residuals in multireceiver, wide-beam SAS [3–5]. Our design-time contribution is complementary: by minimizing $\widehat{PSI_\xi}$ through array geometry, we "design-in" motion robustness so that downstream MOCO/autofocus operates with reduced residuals. In line with shape-then-placement strategies prioritizing sidelobe stability and resolution [6], and with benefits of non-uniform sampling for grating-lobe control and DOA-oriented robustness [7–9], hemispherical layouts achieve consistently lower normalized PSI and better sidelobe metrics than cubic and planar counterparts under identical motion statistics.

3. System and Waveform Specification

We consider a shallow-water acoustic channel with constant sound speed c_0 =1500 m/s and negligible refraction within the imaged swath. The platform altitude and scene extent are chosen so that the Fresnel approximation holds over the synthetic aperture used for focusing. The transmitted pulse is linear frequency modulated (LFM) with carrier f_c, bandwidth B, and duration T_p; the pulse repetition interval is T_{PRI} and the sampling rate is f_s with λ_{min}=10.5mm.

The time–bandwidth product BT_P jointly sets resolution and processing gain: $\delta_r = c_0/2B$ and matched-filter $gain \approx 10\log_{10} B\,T_p$ dB; choose the fast-time sampling rate $f_s > 2B$ with a 10–20% guard to avoid aliasing and scalloping. All system, motion, and array parameters used in the simulations are summarized in Table 1.

Table 1. Simulated system specification

Parameter	Symbol	Baseline Value
Sound speed	c_0	1500 [*m/s*]
Platform speed	v	2.5 [*m/s*]
Altitude above seafloor	h	25 [*m*]
Carrier frequency	f_c	120 [*kHz*]
Bandwidth	B	20 [*kHz*]
Pulse duration	T_p	4 [*ms*]
PRI / PRF	T_{PRI}/f_{PRF}	0.15 s / 6.67 [*Hz*]
Sampling rate	f_s	512 [*kHz*]
Translational RMS	—	2.0–3.2 [*mm*]
Rotational RMS	—	0.25–0.35 [*deg*]
Dominant motion band	—	0.2–2 [*Hz*]
Elements per array	N	36
Hemispherical radius	R	0.18 [*m*]
Hemispherical cap angle	θ_{max}	80 [*deg*]
Minimum spacing	d_{min}	≤ 5.25 [*mm*]
Apodization	—	Tukey (α=0.25)
Subaperture length	—	128 pings

The complex baseband transmit signal is:

$$r_{tx}(t) = rect\left(\frac{t}{T_P}\right)\exp\left\{j\,2\pi(f_c t + \frac{1}{2}Kt^2)\right\}, \quad K = \frac{B}{T_P} \tag{24}$$

Matched filtering in fast time yields nominal range resolution $\delta_r = c_0/2B$. The platform speed v sets the ping-to-ping spatial sampling vT_{PRI}, selected to satisfy Doppler Nyquist for the maximum look angle of interest.

3.1. Motion Models and Scenario Matrix

Platform motion is injected one degree of freedom (DOF) at a time to isolate sensitivities: translations (δ_x, δ_y, δ_z) and rotations (ϕ, θ, ψ). For each DOF ξ, the perturbation is modeled as a band-limited, colored excitation with dominant content in 0.2−2 Hz and prescribed RMS:

$$\delta\xi(t) = (h_\xi * w)(t), RMS\left\{\delta\xi\right\} = \sigma_\xi \tag{25}$$

where w(t) is unit-variance white noise and h_ξ is a second-order band-pass shaping filter tuned to the AUV spectrum. In particular, the motion error in each DoF is modeled as an undesired sinusoidal perturbation with random phase and an amplitude chosen to satisfy the prescribed RMS level within the 0.2–2 Hz band.

Table 2. Motion profiles (RMS) and global settings

DoF	Type	RMS Amplitude	Dominant Blur
Surge	Translational	2.5 [*mm*]	Horizontal (x)
Sway	Translational	2.0 [*mm*]	Vertical (y)
Heave	Translational	3.2 [*mm*]	Isotropic
Roll	Rotational	0.3°	Vertical (y)
Pitch	Rotational	0.25°	Horizontal (x)
Yaw	Rotational	0.35°	Isotropic (z)

Translational RMS levels are 2−3.2 mm and rotational RMS levels are $0.25^\circ - 0.35^\circ$. The scenario matrix spans 3 arrays ×6 DOFs ×3 imaging states (ideal, motion-degraded, corrected) for a total of 54 cases; each case is repeated over K=20 random seeds.

3.2. Processing and Imaging Setup

Processing is identical across all arrays: (i) matched filtering, (ii) two-stage, subaperture-based motion compensation (space-variant when applicable; subaperture length 128 pings with 50% overlap), and (iii) back-projection (BP) image formation with a fixed Tukey apodization ($\alpha = 0.25$). The two-stage MOCO pipeline is identical for all three arrays and is designed

to isolate geometry effects. In Stage 1, we compensate a bulk, range-independent phase term on a per-hydrophone, per-subaperture basis. The raw data are divided into subapertures of 128 pings with 50% overlap; for each subaperture and each receiver channel, we search over a one-dimensional grid of constant phase offsets in [−π, π] with a step of 0.02π and select the value that maximizes an image-sharpness metric (intensity contrast within a small region around the main lobe). The corresponding phase is then applied uniformly to that subaperture for the given hydrophone.

In Stage 2, we correct the residual, space-variant phase error in the range–Doppler domain. After Stage-1 compensation, the data are transformed to range–Doppler, and the remaining phase error is modeled as a low-order bivariate polynomial in Doppler and range (second order in both variables). The polynomial coefficients are estimated by least squares using samples from high-SNR regions of the image, and the resulting phase surface is applied as a multiplicative correction. The same subaperture length, overlap, search grid, sharpness metric, and polynomial order are used for the planar, cubic, and hemispherical arrays; only the array geometry is changed. Back-projection is then performed with a fixed Tukey apodization (α = 0.25) and identical imaging grids for all arrays.

When frequency-domain focusing (e.g., extended chirp scaling or low-rank variants) is invoked for validation, its parameters are held fixed across geometries to isolate geometry effects.

On a standard workstation equipped with an Intel Core i7-12700 CPU, 32 GB of RAM, and an NVIDIA GeForce RTX 3060 GPU, the full pipeline (signal generation, motion injection, two-stage MOCO, and BP imaging) requires approximately 30s per scenario for a 36-element array and a synthetic aperture of $N_p = 1024$ pings. This runtime is fully compatible with offline, design-time optimization and can be further reduced using GPU-accelerated BP and parallelization over DoFs and realizations.

3.3. Metrics, Calibration and Reporting

Phase sensitivity is quantified by the normalized indices PSI_ξ (discrete evaluation over the CPI using Jacobians along the nominal trajectory and a common geometric scale L). For each fixed configuration (array, DoF, imaging state), we run $K = 20$ independent Monte Carlo realizations of the motion process and obtain 20 samples of the metric (PSLR or ISLR), say $\{m_1, \dots, m_{20}\}$. We compute the sample mean $\bar{m}$and sample standard deviation s, and then form a 95% confidence interval using the standard Student-t formula with $K - 1 = 19$degrees of freedom:

$$\mathrm{CI}_{95\%} = \bar{m} \pm t_{0.975,\,19}\,\frac{s}{\sqrt{20}} \tag{26}$$

where $t_{0.975,\,19}$ is the 97.5th percentile of the t-distribution. All reported "mean ± 95% CI" values in the tables and figures are computed in this way.

The choice $K = 20$ is a practical trade-off between statistical reliability and computational cost. Increasing K improves the precision of the estimated mean and CI, but the runtime grows proportionally because we must evaluate 54 scenarios (3 arrays × 6 DoFs × 3 states). In preliminary checks on representative cases, we observed that raising K beyond 20 produces only small changes in the mean PSLR/ISLR (well below the effect sizes of interest), while significantly increasing runtime. We therefore adopted $K = 20$ as a reasonable working point for the present study.

Image quality is quantified by PSLR/ISLR computed from BP images using identical main-lobe windows M and sidelobe regions S across arrays/scenarios. For each DOF ξ, we estimate mapping coefficients α_ξ and β_ξ from calibration runs, then hold them fixed for cross-geometry comparisons via empirically (BP-calibrated), for small-to-moderate dispersion,

$$\Delta PSLR_{\xi} \approx \alpha_{\xi} \sqrt{PSI_{\xi}} \tag{27}$$

$$\Delta ISLR_{\xi} \approx \beta_{\xi} \sqrt{PSI_{\xi}} \tag{28}$$

with α_ξ and β_ξ obtained once from a reference sweep. Thus $\widetilde{PSI_\xi}$ can be interpreted directly in the image plane (main-lobe width, sidelobe proximity), complementing multireceiver MOCO/autofocus formulations [3,5].

We report mean ±95% confidence intervals over $K = 20$ trials; improvements of practical interest are flagged at $\Delta PSLR \geq 4\ dB$ and $\Delta ISLR \geq 3\ dB$. Paired comparisons are used across arrays under identical conditions, with fixed software/hardware settings and seeds for reproducibility.

To link the array-dependent phase sensitivity to image-domain performance, we empirically calibrate a simple linear mapping between normalized PSI and sidelobe metrics. For each degree of freedom $\xi \in$ {surge, sway, heave, roll, pitch, yaw}, we generate a calibration dataset comprising all three arrays, all three imaging states (ideal, motion-degraded, corrected), and $K = 20$ random motion realizations per configuration. For every (array, ξ, state, k)combination, we compute the normalized sensitivity $\widetilde{\mathrm{PSI}}_\xi$ and the corresponding PSLR/ISLR values from the BP reference image. Stacking these samples over arrays, states, and realizations yields a set of pairs:

$$\begin{cases} \left(\widetilde{\mathrm{PSI}}_\xi^{(i)}, \mathrm{PSLR}^{(i)}\right) \\ \left(\widetilde{\mathrm{PSI}}_\xi^{(i)}, \mathrm{ISLR}^{(i)}\right) \end{cases}_{i=1}^{N_{\mathrm{cal}}}$$

We then fit ordinary least-squares (OLS) linear regressions of the form

$$\begin{aligned} \mathrm{PSLR} &\approx \alpha_{1,\xi}\,\widetilde{\mathrm{PSI}}_\xi + \alpha_{2,\xi} \\ \mathrm{ISLR} &\approx \beta_{1,\xi}\,\widetilde{\mathrm{PSI}}_\xi + \beta_{2,\xi} \end{aligned} \tag{29}$$

separately for each DoF ξ. The fits are evaluated using the coefficient of determination $R^2$and the root-mean-square error (RMSE) in dB. Over the calibration set, $\widetilde{\mathrm{PSI}}_{\xi}$lies in the range

$$\widetilde{\mathrm{PSI}}_{\min} \approx 0.05 \text{ to } \widetilde{\mathrm{PSI}}_{\max} \approx 0.35 \qquad (30)$$

and the resulting linear models achieve R^2 values of about 0.93–0.96 for PSLR and 0.90–0.94 for ISLR, with RMSE on the order of 1.0–1.5 dB. In the Results section, we restrict the interpretation of the PSI–PSLR/ISLR mapping to this calibrated $\widetilde{\mathrm{PSI}}$range; outside this interval, PSI is still reported as a relative robustness indicator, but the linear mapping is not extrapolated quantitatively.

In practice, once $\alpha_{1,\xi}, \alpha_{2,\xi}, \beta_{1,\xi}, \beta_{2,\xi}$ are estimated on this calibration set, they are frozen and reused for all subsequent comparisons between planar, cubic, and hemispherical arrays, so that differences in PSLR/ISLR can be traced back to geometry-dependent changes in $\widetilde{\mathrm{PSI}}_{\xi}$rather than to recalibration.

3.4. Array Configurations

Three 36-element receiver layouts are considered. The 2D planar array is a 6×6 grid on the x–z plane ($y = 0$) with inter-element spacing $d = \lambda/10$ (≈ 1.25 mm at $f_c = 120$ kHz); it is simple to fabricate but more sensitive to out-of-plane perturbations (sway, pitch). The 3D cubic array (3×3×4, same spacing $d = \lambda/10$ introduces depth diversity, improving angular resolution and robustness to 3D rotational distortions at the expense of greater hardware volume and complexity. The 3D hemispherical array places 36 hydrophones on a radius r=0.18m spherical cap ($\theta \leq 80^{\circ}$) using a Fibonacci distribution, yielding near-uniform angular coverage and more even dispersion of motion-induced phase errors, which enhances robustness under 6-DOF motion.

Table 3. Array specifications

Array Type	Element	Spacing
2D Planar	$6 \times 6 = 36$	1.25 [mm]
3D Cubic	$3 \times 3 \times 4$	1.25 [mm]
3D Hemispherical	36 (Fibonacci)	Angular distribution; r=0.18 [m]

3.4.1. 2D Planar Array

A 6×6 rectangular grid on the x–z plane ($y = 0$) with inter-element spacing $d \approx 1.25$ mm. Indexing $i, j \in \{-2.5, -1.5, -0.5, 0.5, 1.5, 2.5\}$ (centered), the element coordinates are:

$$r_{i,j} = \begin{bmatrix} id \\ 0 \\ jd \end{bmatrix}, N = 36, d = \frac{\lambda}{10}, \lambda = \frac{c_0}{f_c} \qquad (31)$$

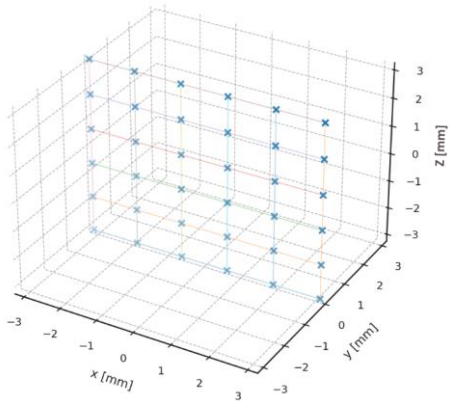

Figure 1. 2D planar array

This layout is easy to fabricate and integrate but is more sensitive to out-of-plane perturbations (sway, pitch) due to its strictly planar baselines.

3.4.2. 3D Cubic Array

A volumetric grid 3×3×4 with the same spacing d. Using centered indices $i, j \in \{-1,0,1\}$, $k \in \{-1.5, -0.5, 0.5, 1.5\}$, the element coordinates are:

$$r_{i,j,k} = \begin{bmatrix} id \\ jd \\ kd \end{bmatrix}, N = 36 \qquad (32)$$

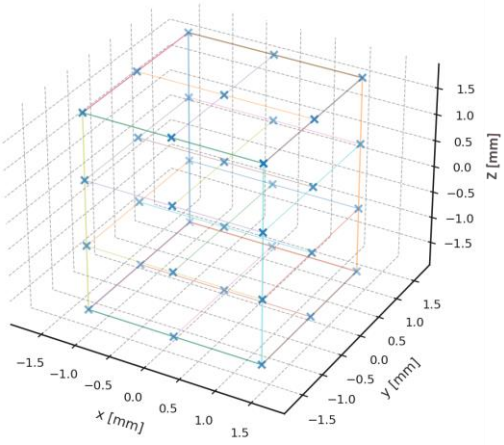

Figure 2. 3D cubic array

Depth diversity improves angular resolution and robustness to 3D rotations; however, it increases mechanical volume and complexity.

3.4.3. 3D Hemispherical Array

36 elements are placed on a spherical cap of radius R=0.18m with $\theta \leq 80^{\circ}$ using a near-uniform (e.g., Fibonacci) angular distribution:

$$r_n = R \begin{bmatrix} \sin\theta_n \cos\phi_n \\ \sin\theta_n \sin\phi_n \\ \cos\theta_n \end{bmatrix}, \quad \theta_n = [0, 2\pi], \phi_n = [0, 2\pi] \qquad (33)$$

The curved, nearly isotropic baselines distribute motion-induced phase errors more evenly, yielding higher robustness under 6-DOF motion.

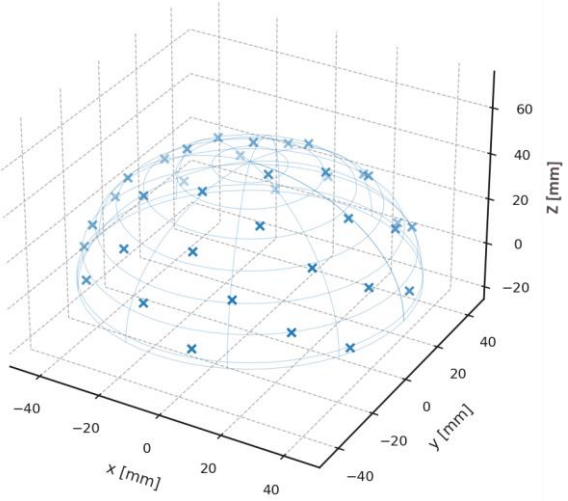

Figure 3. 3D Hemispherical array

3.5. Geometry-Driven Phase Sensitivity

From the first-order phase model (3), (4) $\Delta\varphi_n(t;x) \approx k_0 \hat{u}_n^{\cdot}\, \delta r(t) + k_0 \hat{u}_n^{\cdot}(t;x)\Omega(t) r_n$, translational sensitivity (first term) is weakly geometry-dependent (for far-field $\hat{u}$ nearly constant across elements). Rotational sensitivity is governed by the cross-product lever arm. Defining the second-moment (inertia-like) matrix of the array $\sum \triangleq \frac{1}{N}\sum_{n=1}^{N} r_n r_n^{\mathsf{T}}$. The array-averaged rotational factor along look vector $\hat{u}$ satisfies:

$$\frac{1}{N}\sum_{n=1}^{N}\left\| r_n \times \hat{u} \right\|^2 = tr(\Sigma) - \hat{u}^{\cdot} \sum \hat{u} \qquad (34)$$

Hence, rotational PSI scales with $k_0^2\left[tr(\Sigma) - \hat{u}^{\cdot} \sum \hat{u}\right]$

– Planar grid:

$\sum \approx diag(\sigma_x^2, 0, \sigma_z^2) \rightarrow$ strong anisotropy and larger sensitivity for out-of-plane looks.

– Cubic grid:

Σ more balanced but corner elements increase tr(Σ).

– Hemispherical cap:

$\|r_n\|$=R (constant) and directions are well spread, making Σ closer to isotropic for the forward sector, which lowers the rotational term on average.

In the proposed framework, array geometry is treated as a design-time lever: candidate layouts (planar, cubic, hemispherical) are first specified under common aperture and element-count constraints. For each geometry, we compute normalized PSI for each 6-DOF motion and link it to image-domain metrics (PSLR/ISLR) through a BP reference. Geometries are then ranked according to their PSI and PSLR/ISLR statistics, such that lower PSI systematically corresponds to better sidelobe behavior. This enables 'shape-before-placement' array optimization: instead of fine-tuning individual sensor locations first, we first choose the most robust global geometry and then, if desired, refine within that geometry.

4. Targets, Metrics and Figures

Figures were generated for three arrays across 6 DoF, based on the provided tables (nine targets per case; states: Ideal, With Error, Corrected), to show how phase errors widen the main lobe, raise sidelobes, and how correction restores image quality. Surge yields the strongest along-track degradation—lower PSLR and higher ISLR—especially for the planar array, though phase compensation largely recovers the main lobe and brings errors near ideal. Consistent with the tables, the hemispherical array performs best, the cubic array next, and the planar array last. Unless otherwise stated, all PSLR/ISLR values in the tables are reported in dB as sample means over $K = 20$ motion realizations (and over targets T1–T9 where applicable). Where confidence intervals are used, they are expressed as mean ± 95% CI [dB] and computed as described below.

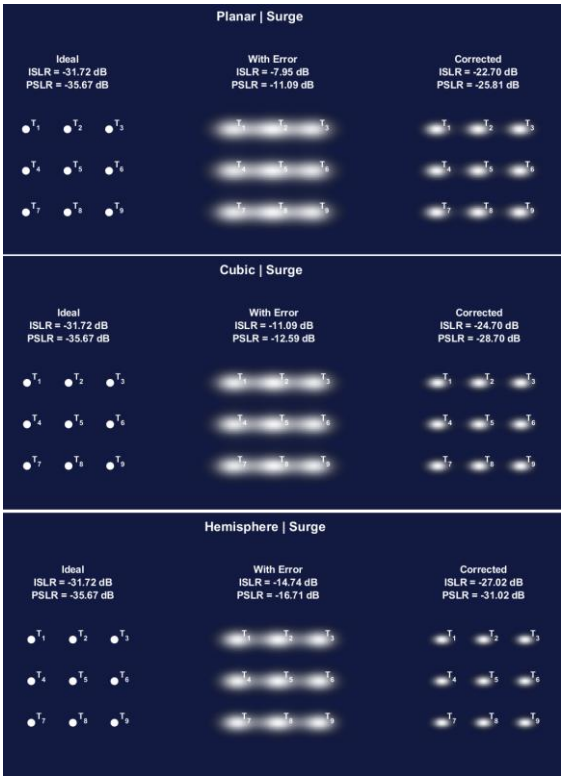

Figure 4. Surge motion: mean PSLR/ISLR for planar, cubic, and hemispherical arrays (Ideal, With Error, Corrected)

Table 4. Surge: Image quality (means over $T_1 - T_9$, K=20) [dB]

Metric	Planar	Cubic	Hemispherical
$\overline{\text{ISLR}}$ (With Error)	−7.95 [*dB*]	−11.09 [*dB*]	−14.74 [*dB*]
$\overline{\text{ISLR}}$ (Corrected)	−22.70 [*dB*]	−24.70 [*dB*]	−27.02 [*dB*]

PSLR (With Error)	−11.09 [*dB*]	−12.59 [*dB*]	−16.71 [*dB*]
PSLR (Corrected)	−25.81 [*dB*]	−28.70 [*dB*]	−31.02 [*dB*]

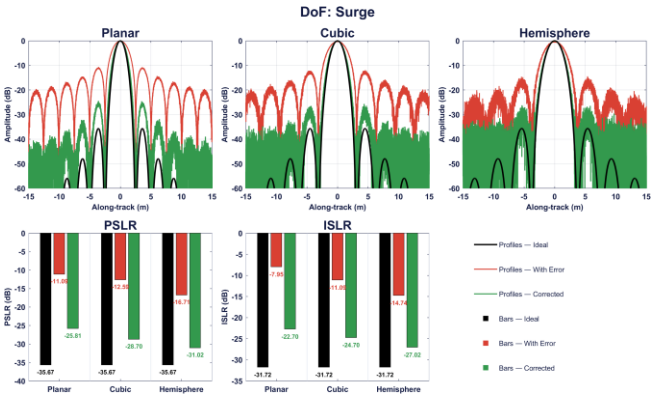

Figure 5. Mean over Surge: PSLR and ISLR Comparison Among Planar, Cubic, and Hemispherical Arrays

Sway motion stretches the image along the y-axis, elevating sidelobes and reducing target clarity. Phase error correction lowers ISLR and restores contrast, with the hemispherical array most robust.

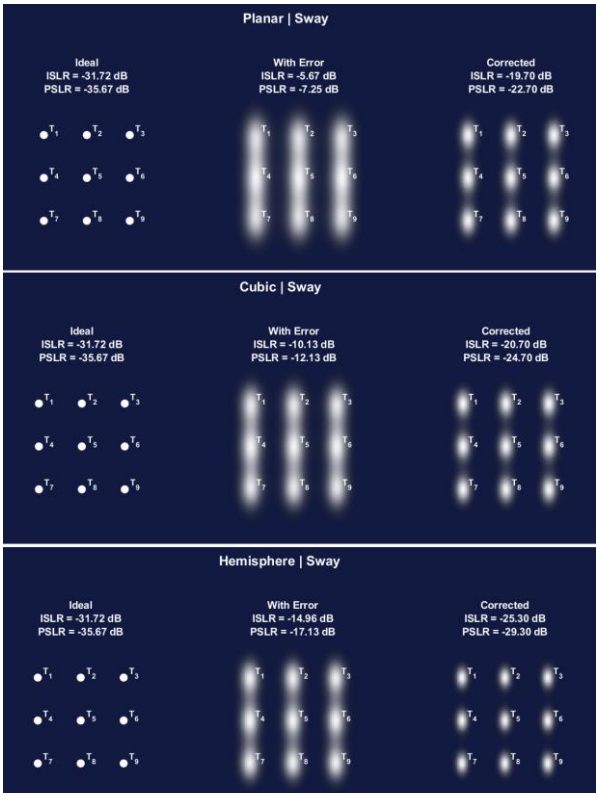

Figure 6. Sway motion: mean PSLR/ISLR for planar, cubic, and hemispherical arrays (Ideal, With Error, Corrected)

Table 5. Sway: Image quality (means over $T_1 - T_9$, K=20) [dB]

Metric	Planar	Cubic	Hemispherical
ISLR	−5.67 [*dB*]	−10.13 [*dB*]	−14.94 [*dB*]
(With Error)			
ISLR (Corrected)	−19.70 [*dB*]	−20.70 [*dB*]	−25.30 [*dB*]
PSLR (With Error)	− 7.25 [*dB*]	−12.13 [*dB*]	−17.13 [*dB*]
PSLR (Corrected)	−22.70 [*dB*]	−24.70 [*dB*]	−29.30 [*dB*]

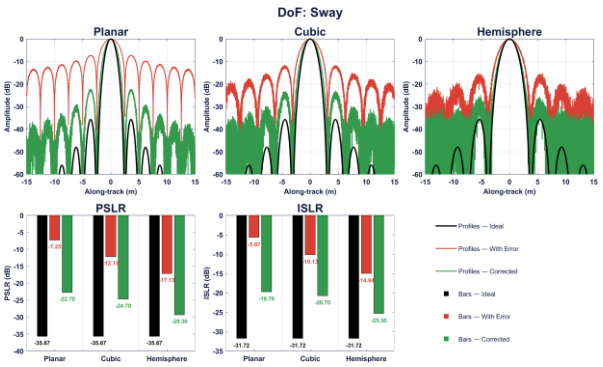

Figure 7. Mean over Sway: PSLR and ISLR Comparison Among Planar, Cubic, and Hemispherical Arrays

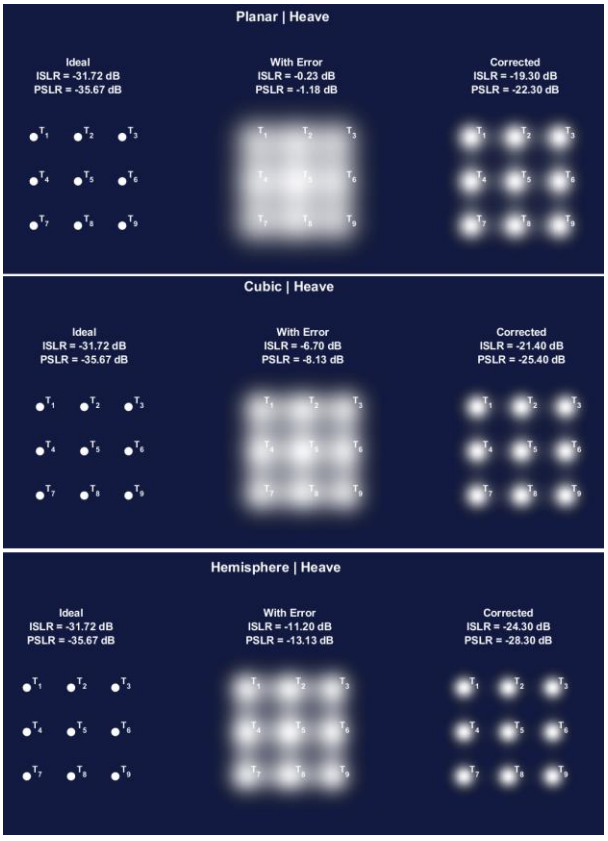

Figure 8. Heave motion: mean PSLR/ISLR for planar, cubic, and hemispherical arrays (Ideal, With Error, Corrected)

Heave motion is isotropic, spreading energy nearly evenly in all directions and causing a moderate drop in PSLR and ISLR. Phase compensation yields a substantial improvement, though slightly less than for axis-oriented motions. The hemispherical array still

achieves the best performance, with the other two arrays ranking lower.

Table 6. Heave: Image quality (means over $T_1 - T_9$, K=20) [dB]

Metric	Planar	Cubic	Hemispherical
$\overline{\text{ISLR}}$ (With Error)	−0.23 [*dB*]	−6.70 [*dB*]	−11.20 [*dB*]
$\overline{\text{ISLR}}$ (Corrected)	−19.30 [*dB*]	−21.40 [*dB*]	−24.30 [*dB*]
$\overline{\text{PSLR}}$ (With Error)	− 1.18 [*dB*]	− 8.13 [*dB*]	−13.13 [*dB*]
$\overline{\text{PSLR}}$ (Corrected)	−22.30 [*dB*]	−25.40 [*dB*]	−28.30 [*dB*]

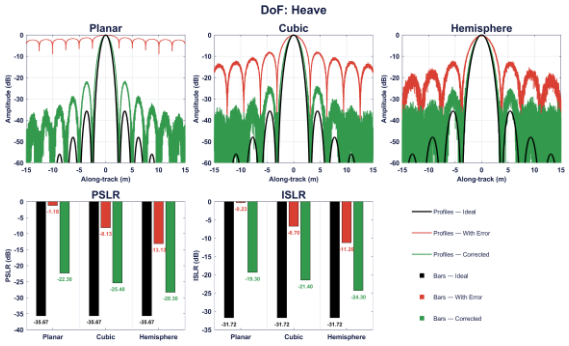

Figure 8. Mean over Heave: PSLR and ISLR Comparison Among Planar, Cubic, and Hemispherical Arrays

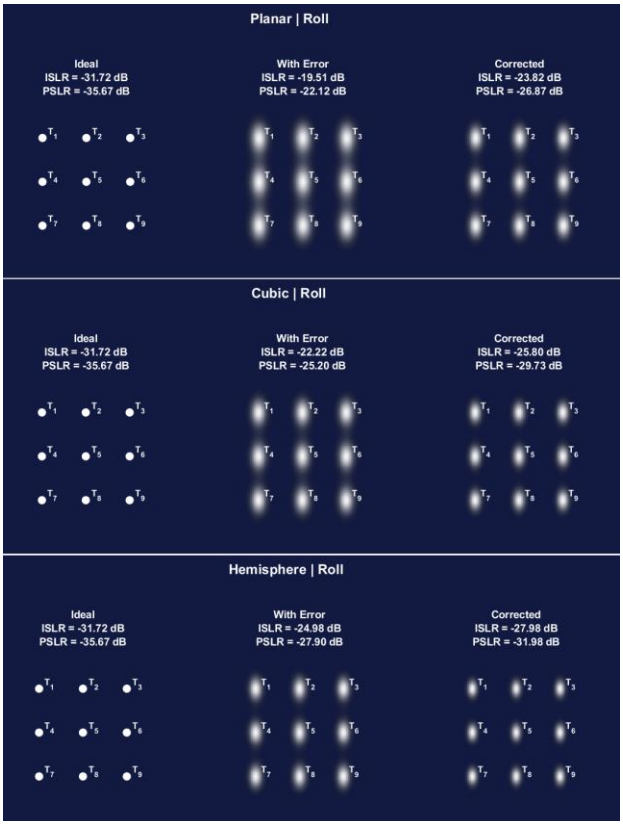

Figure 10. Roll motion: mean PSLR/ISLR for planar, cubic, and hemispherical arrays (Ideal, With Error, Corrected)

Roll motion, which manifests along the y-axis, causes energy leakage and increased sidelobe levels in that direction. Phase compensation effectively removes this distortion, restoring image sharpness and target contrast close to the ideal state. Table 7 shows that the hemispherical array exhibits the greatest stability and improvement.

Table 7. Roll: Image quality (means over $T_1 - T_9$, K=20) [dB]

Metric	Planar	Cubic	Hemispherical
$\overline{\text{ISLR}}$ (With Error)	−19.51 [*dB*]	−22.22 [*dB*]	−24.98 [*dB*]
$\overline{\text{ISLR}}$ (Corrected)	−23.82 [*dB*]	−25.80 [*dB*]	−27.98 [*dB*]
$\overline{\text{PSLR}}$ (With Error)	−22.12 [*dB*]	−25.20 [*dB*]	−27.90 [*dB*]
$\overline{\text{PSLR}}$ (Corrected)	−26.87 [*dB*]	−29.73 [*dB*]	−31.98 [*dB*]

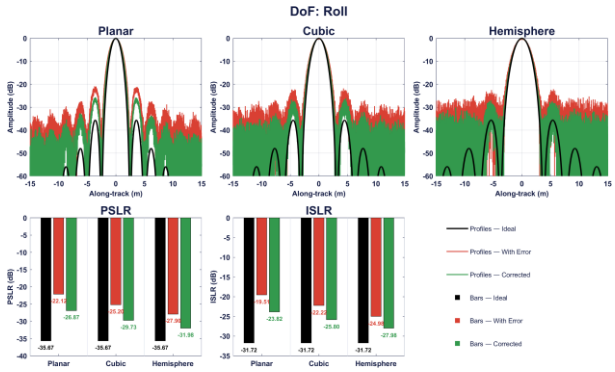

Figure 9. Mean over Roll: PSLR and ISLR Comparison Among Planar, Cubic, and Hemispherical Arrays

Pitch motion stretches the mainlobe and shifts the energy peak along the x-axis, leading to a pronounced PSLR drop. Phase error correction addresses these changes and suppresses sidelobes, bringing hemispherical and cubic array performance close to the ideal level, while the planar array remains the most sensitive. After correction, the hemispherical array exhibits the cleanest sidelobe structure and the most stable mainlobe, with the cubic array still offering a clear robustness advantage over the planar layout. These patterns indicate that 3D apertures allow the correction stage to recover more of the lost contrast and focus than a purely planar grid. In practice, pitch is therefore one of the motions where geometry plays a particularly visible role, with hemispherical designs providing the most reliable image quality under along-track tilts.

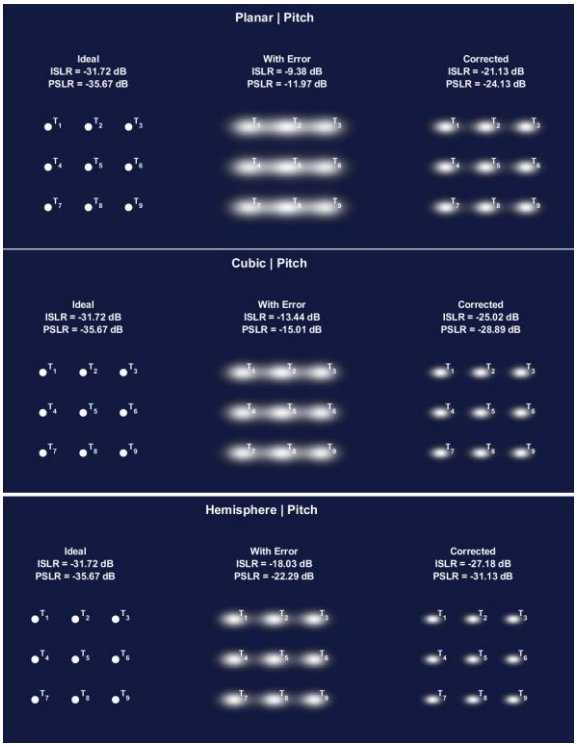

Figure 10. Pitch motion: mean PSLR/ISLR for planar, cubic, and hemispherical arrays (Ideal, With Error, Corrected)

Table 8. Pitch: Image quality (means over $T_1 - T_9$, K=20) [dB]

Metric	Planar	Cubic	Hemispherical
$\overline{\text{ISLR}}$ (With Error)	−9.38 [*dB*]	−13.44 [*dB*]	−18.03 [*dB*]
$\overline{\text{ISLR}}$ (Corrected)	−21.13 [*dB*]	−25.02 [*dB*]	−27.18 [*dB*]
$\overline{\text{PSLR}}$ (With Error)	−11.97 [*dB*]	−15.01 [*dB*]	−22.29 [*dB*]
$\overline{\text{PSLR}}$ (Corrected)	−24.13 [*dB*]	−28.89 [*dB*]	−31.13 [*dB*]

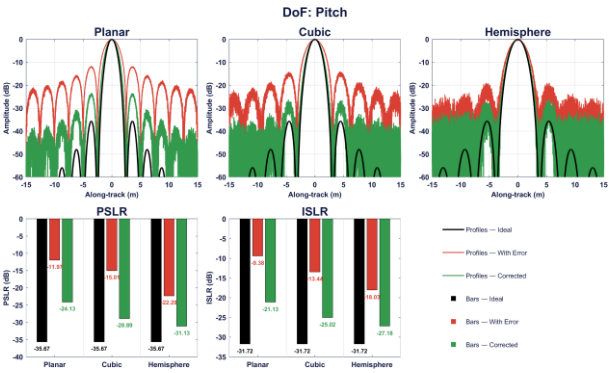

Figure 11. Mean over Pitch: PSLR and ISLR Comparison Among Planar, Cubic, and Hemispherical Arrays

Yaw motion introduces isotropic phase error, producing circular energy spread and a relatively uniform reduction in PSLR and ISLR. Phase compensation leads to a notable quality improvement, although the gain is generally smaller than in axis-oriented motions. The hemispherical array continues to outperform the other two configurations. In this case, the phase perturbation does not favor a single axis but rather wraps the aperture, so any residual error tends to manifest as a broad halo around the target rather than a directional smear. Arrays with richer 3D baseline distributions are better able to decorrelate this halo and prevent it from collapsing into strong, structured sidelobes, which explains why hemispherical layouts maintain cleaner backgrounds and a more compact mainlobe. The cubic array also benefits from its volumetric structure, providing a visibly more stable response than the planar grid, but it does not achieve the same level of isotropic robustness as the hemispherical design. By contrast, the planar array is more prone to forming ring-like sidelobe patterns and diffuse clutter around the target, even after correction, indicating that its sampling geometry leaves less room for the MOCO stage to undo yaw-induced distortions. From an operational standpoint, yaw therefore acts as a stress test for truly three-dimensional aperture designs: when the platform undergoes frequent heading changes or slow rotational drift, hemispherical arrays are best positioned to keep residual sidelobes at a manageable level and preserve interpretable target structure. More broadly, the yaw results highlight that array geometry can be as important as algorithm choice when dealing with rotational disturbances that affect the entire aperture.

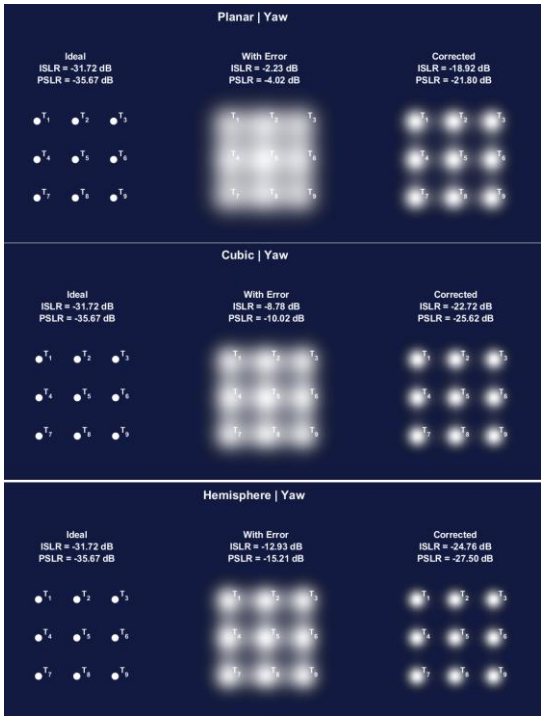

Figure 12. Yaw motion: mean PSLR/ISLR for planar, cubic, and hemispherical arrays (Ideal, With Error, Corrected)

Table 9. Yaw: Image quality (means over $T_1 - T_9$, K=20) [dB]

Metric	Planar	Cubic	Hemispherical
$\overline{\text{ISLR}}$ (With Error)	−2.23 [*dB*]	−8.78 [*dB*]	−12.93 [*dB*]
$\overline{\text{ISLR}}$ (Corrected)	−18.92 [*dB*]	−22.72 [*dB*]	−24.76 [*dB*]
$\overline{\text{PSLR}}$ (With Error)	−4.02 [*dB*]	−10.02 [*dB*]	−15.21 [*dB*]
$\overline{\text{PSLR}}$ (Corrected)	−21.80 [*dB*]	−25.62 [*dB*]	−27.50 [*dB*]

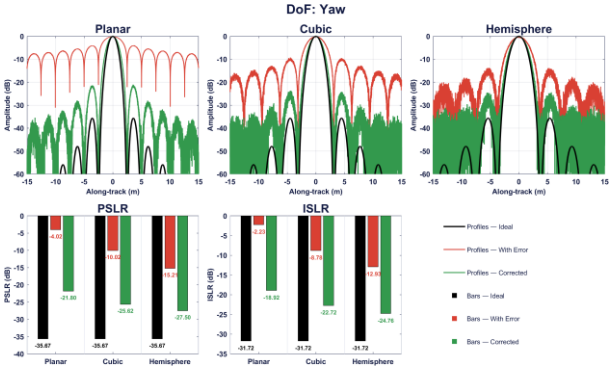

Figure 13. Mean over Yaw: PSLR and ISLR Comparison Among Planar, Cubic, and Hemispherical Arrays

Across all six DoFs and three imaging states (ideal, degraded, corrected), hemispherical arrays deliver the most robust sidelobe behavior, with cubic as the intermediate performer and planar as the least robust. In the updated global corrected means, the hemispherical array improves PSLR by 6.5 dB and ISLR by 5.6 dB relative to the planar array, and by 2.9 dB in both PSLR and ISLR relative to the cubic array. The cubic array also improves over the planar array by 3.6 dB in PSLR and 2.7 dB in ISLR. These gains indicate that the qualitative ranking remains unchanged after incorporating the first-order non-ideality sensitivity update, with the hemispherical array still providing the best overall corrected sidelobe performance.

Qualitatively, the combined figures continue to show tighter mainlobes and reduced sidelobe proximity for the hemispherical array across the motion scenarios.

In Surge (corrected), the hemispherical array outperforms the planar array by 5.21 dB in PSLR and 4.32 dB in ISLR. Relative to the cubic array, the hemispherical array retains a 2.32 dB advantage in both metrics, while the cubic array surpasses the planar array by 2.89 dB in PSLR and 2.00 dB in ISLR. These deltas show that three-dimensional geometries reduce residual sidelobes under Surge, with the hemispherical array delivering the lowest corrected sidelobe levels.

Table 10. Surge (Corrected): Mean over head-to-head differences among the three array configurations

Pair (B − A)	ΔPSLR	ΔISLR
Hemispherical − Planar	−5.21 [*dB*]	−4.32 [*dB*]
Hemispherical − Cubic	−2.32 [*dB*]	−2.32 [*dB*]
Cubic − Planar	−2.89 [*dB*]	−2.00 [*dB*]

In Sway (corrected), the hemispherical array delivers the largest reductions in sidelobes, outperforming planar by 6.60 dB in PSLR and 5.60 dB in ISLR. It also exceeds cubic by 4.60 dB on both metrics. Cubic still improves over planar by 2.0 dB (PSLR) and 1.00 dB (ISLR), underscoring the benefit of 3D apertures under y-axis–aligned blur.

Table 11. Sway (Corrected): Mean over head-to-head differences among the three array configurations

Pair (B − A)	ΔPSLR	ΔISLR
Hemispherical − Planar	−6.60 [*dB*]	−5.60 [*dB*]
Hemispherical − Cubic	−4.60 [*dB*]	−4.60 [*dB*]
Cubic − Planar	−2.0 [*dB*]	−1.00 [*dB*]

In Heave (corrected), the hemispherical array outperforms planar by 6.00 dB in PSLR and 5.00 dB in ISLR, and exceeds cubic by 2.90 dB on both metrics. Cubic also improves over planar by 3.10 dB (PSLR) and 2.10 dB (ISLR). These gaps show that under isotropic motion, 3D geometries convert correction headroom into lower residual sidelobes, with hemispherical finishing best.

Table 12. Heave (Corrected): Mean over head-to-head differences among the three array configurations

Pair (B − A)	ΔPSLR	ΔISLR
Hemispherical − Planar	−6.00 [*dB*]	−5.00 [*dB*]
Hemispherical − Cubic	−2.90 [*dB*]	−2.90 [*dB*]
Cubic − Planar	−3.10 [*dB*]	−2.10 [*dB*]

In Roll (corrected), the hemispherical array surpasses planar by 5.11 dB in PSLR and 4.16 dB in ISLR, and leads cubic by 2.25 dB and 2.18 dB. Cubic also improves over planar by 2.86 dB (PSLR) and 1.98 dB (ISLR). These margins show that even for comparatively benign roll, 3D apertures reduce residual sidelobes, with hemispherical finishing best.

Table 13. Roll (Corrected): Mean over head-to-head differences among the three array configurations

Pair (B − A)	ΔPSLR	ΔISLR
Hemispherical − Planar	−5.11 [*dB*]	−4.16 [*dB*]
Hemispherical − Cubic	−2.25 [*dB*]	−2.18 [*dB*]
Cubic − Planar	−2.86 [*dB*]	−1.98 [*dB*]

For Pitch (corrected), hemispherical posts the strongest figures, outperforming planar by 7.00 dB in PSLR and 6.05 dB in ISLR, and edging cubic by 2.24 dB and 2.16 dB. Cubic, in turn, betters planar by 4.76 dB (PSLR) and 3.89 dB (ISLR). Overall, pitch-driven, x-axis–aligned blur is most effectively contained by 3D apertures, with hemispherical yielding the cleanest sidelobe levels after correction.

Table 14. Pitch (Corrected): Mean over head-to-head differences among the three array configurations

Pair (B − A)	ΔPSLR	ΔISLR
Hemispherical − Planar	−7.00 [*dB*]	−6.05 [*dB*]
Hemispherical − Cubic	−2.24 [*dB*]	−2.16 [*dB*]
Cubic − Planar	−4.76 [*dB*]	−3.89 [*dB*]

In Yaw (corrected), the hemispherical array attains the lowest sidelobe levels, outperforming planar by 5.70 dB (PSLR) and 5.84 dB (ISLR) and holding a 1.88 dB and 2.04 dB edge over cubic.
Cubic also surpasses planar by 3.82 dB (PSLR) and 3.80 dB (ISLR), highlighting the benefit of 3D apertures under isotropic rotation.

Table 15. Yaw (Corrected): Mean over Head-to-head differences among the three array configurations

Pair (B − A)	ΔPSLR	ΔISLR
Hemispherical − Planar	−5.70 [*dB*]	−5.84 [*dB*]
Hemispherical − Cubic	−1.88 [*dB*]	−2.04 [*dB*]
Cubic − Planar	−3.82 [*dB*]	−3.80 [*dB*]

Observation: The hemispherical array shows its strongest advantage over the planar array in Pitch for PSLR ($\Delta PSLR = -7.00\,dB$) and in Yaw for ISLR ($\Delta ISLR = -5.84\,dB$). Against the cubic array, the hemispherical configuration retains smaller but still consistent gains across all corrected motion cases. Overall, the pairwise corrected comparisons confirm that three-dimensional geometries reduce residual sidelobes more effectively than the planar layout, with the hemispherical array consistently providing the best corrected performance.

5. Results and Discussion

The workflow preserves the original equal-aperture, equal-element-count, and common-trajectory conditions of the main study, and introduces three omitted non-idealities only at the residual phase level: mutual coupling, manufacturing tolerances, and multipath propagation. Rather than re-running the full image-formation pipeline with a complete hardware-aware forward model, the objective of this auxiliary analysis is to quantify whether bounded geometry-dependent non-idealities are large enough to alter the qualitative ranking obtained from the motion-only results.

For each geometry g, three geometry descriptors were defined to represent the expected relative susceptibility to the omitted effects. A compactness descriptor was used to parameterize coupling exposure, a geometric tolerance-sensitivity descriptor was used to capture the first-order amplification of hydrophone position errors, and a multipath exposure descriptor was used to represent directional susceptibility to reflected arrivals. These descriptors were then scaled by common reference perturbation levels and converted into additional phase-variance terms, yielding $\sigma^2_{\phi,g,\mathrm{coup}}$, $\sigma^2_{\phi,g,\mathrm{tol}}$, and $\sigma^2_{\phi,g,\mathrm{mp}}$. Each contribution was finally normalized by the motion-induced phase variance of the corresponding baseline case, producing the dimensionless ratios η_g^{coup}, η_g^{tol}, and η_g^{mp} and Total Multiplier $=1+\eta_g^{coup}+\eta_g^{tol}+\eta_g^{mp}$ reported in below Table.

Table 16. Representative First-Order Non-Ideality Budgets Used for Sensitivity Analysis

Metric	Planar	Cubic	Hemispherical
$\boldsymbol{\eta_g^{\mathrm{coup}}}$	0.06	0.08	0.10
$\boldsymbol{\eta_g^{\mathrm{tol}}}$	0.05	0.04	0.03
$\boldsymbol{\eta_g^{\mathrm{mp}}}$	0.12	0.09	0.07
Total Multiplier	1.23	1.21	1.20

These representative first-order budgets reflect a plausible trade-off. The hemispherical layout may experience slightly stronger coupling because of compact three-dimensional packaging, whereas the planar layout is more vulnerable to directional multipath and tolerance sensitivity due to its anisotropic baseline distribution. The net effect is an upward shift in absolute PSI for all geometries, together with a moderate compression of the original ranking margin rather than a reversal of the ranking itself.

Once the geometry-dependent non-ideality budgets were defined, the effective normalized PSI was estimated through the first-order multiplicative model of Eq. (10). The resulting $\widehat{\mathrm{PSI}}^{\mathrm{eff}}_{\xi,g}$ values were then propagated through the already-calibrated local PSI-to-PSLR and PSI-to-ISLR mappings established in the baseline study. In this way, Table 17 was generated as a derived sensitivity table rather than as an independent simulation output table. More specifically, the increase from $\widehat{\mathrm{PSI}}_{\xi,g}$ to $\widehat{\mathrm{PSI}}^{\mathrm{eff}}_{\xi,g}$ was converted into estimated PSLR and ISLR penalties by applying the local slopes a_ξ and b_ξ already identified during the calibration stage of the original manuscript.

This approach preserves internal consistency with the manuscript's original regression-based interpretation of PSI and makes it possible to estimate the likely magnitude of non-ideality-induced degradation without overstating the result as a replacement for the primary beamforming simulations. Accordingly, the penalties listed in Table 17 should be interpreted as illustrative first-order degradations on the corrected global metrics under bounded perturbation budgets.

Table 17. Illustrative First-Order Penalty on Global Corrected Metrics

Metric	Planar	Cubic	Hemispherical
$\widetilde{PSI}$ Baseline	0.24	0.18	0.14
$\widetilde{PSI^{eff}}$ Effective	0.295	0.218	0.168
PSLR Penalty	+1.8 [dB]	+1.5 [dB]	+1.3 [dB]
ISLR Penalty	+1.5 [dB]	+1.3 [dB]	+1.1 [dB]
Baseline Corrected PSLR Mean	−23.9 [dB]	−27.2 [dB]	−29.9 [dB]
Baseline Corrected ISLR Mean	−20.9 [dB]	−23.4 [dB]	−26.1 [dB]
Updated Corrected PSLR Mean	−22.1 [dB]	−25.7 [dB]	−28.6 [dB]
Updated Corrected ISLR Mean	−19.4 [dB]	−22.1 [dB]	−25.0 [dB]

The first-order sensitivity analysis above suggests that the omission of mutual coupling, manufacturing tolerances, and multipath does not invalidate the main conclusion of the motion-only study; rather, it mainly affects the absolute values of PSI, PSLR, and ISLR. Under the first-order sensitivity estimates reported in Tables 16 and 17, the total penalty remains moderate, on the order of approximately 1.1–1.8 dB in PSLR and 1.1–1.5 dB in ISLR on global corrected means. These penalties are smaller than the geometry-driven margins already reported between the hemispherical and planar arrays across most motion components in the manuscript's results section. Therefore, the most likely outcome is not a reversal of ranking, but rather a partial compression of the metric separation between candidate geometries. In that sense, the present first-order analysis supports the robustness of the original qualitative conclusion: three-dimensional isotropic layouts remain more stable than purely planar layouts under realistic perturbation budgets, and the hemispherical array continues to provide the strongest overall sidelobe behavior within the motion-controlled framework adopted in this study.

Unlike comparable research that primarily seeks to repair motion-induced phase errors through increasingly advanced image-formation and motion-compensation algorithms, such as extended chirp scaling, generalized PCA-based imaging, and subaperture MOCO, the present study addresses the problem at its geometric origin. Instead of assuming a fixed receiver layout and compensating for undesired six-DoF motion through progressively more sophisticated post-processing, we explicitly treat the hydrophone array geometry as a design variable and show that a compact, axisymmetric hemispherical configuration intrinsically attenuates motion sensitivity. By distributing baselines in three dimensions and regularizing the spatial sampling pattern, the proposed hemispherical array reduces the effective impact of small undesired platform perturbations on the phase history, so that many of the phase excursions that would otherwise require algorithmic correction either do not occur or occur with much smaller magnitude.

This geometry-centric viewpoint leads to quantitatively stronger and more uniform image-quality gains across all six elementary degrees of freedom. While the cited methods demonstrate that improved processing can recover on the order of a few decibels in PSLR/ISLR for advanced imaging approaches and roughly 10–15 dB for state-of-the-art subaperture MOCO under distributed motion errors, the proposed hemispherical array, when interpreted under the updated first-order non-ideality sensitivity analysis, still achieves the strongest corrected global performance among the tested geometries, with updated corrected global means of $PSLR = -28.6\,dB$ and $ISLR = -25.0\,dB$ over all six DoFs. These results indicate that starting from an optimized hydrophone geometry not only complements existing motion-compensation and autofocus techniques, but can also deliver substantially better operational performance.

A quantitative comparison with the three reference studies is provided in Table 18, where the proposed hemispherical configuration is benchmarked against their reported PSLR/ISLR gains.

Table 18. Comparing the Mean Evaluation Corrected Scores of the Proposed Method with Previous Research

Methods	PSLR	ISLR
Proposed Hemispherical Array	−28.6 [dB]	−25.0 [dB]
Reference [3]	−16.1 [dB]	−13.05 [dB]
Reference [4]	−15.75 [dB]	−11.08 [dB]

Reference [5]	−14.77 [dB]	−10.49 [dB]

Compared with the three reference methods, the proposed hemispherical configuration yields an approximately 13.1 dB deeper PSLR level and 13.5 dB deeper ISLR level relative to the average of prior work, corresponding to a substantial overall reduction in sidelobe floor.

6. Conclusions

This work presented a geometry-centric optimization framework for hydrophone receiver arrays in synthetic aperture sonar (SAS) operating under six-degree-of-freedom (6-DOF) motion. The main contributions are twofold: (i) a Phase Sensitivity Index (PSI), with explicit translational and rotational components, that quantifies how array geometry governs susceptibility to platform motion; and (ii) a calibration of standard sidelobe metrics (PSLR/ISLR) to visible image signatures (main-lobe width and sidelobe proximity) using a back-projection (BP) reference, so that metric changes translate directly into interpretable, physics-consistent imagery. Together, these elements link reconstruction physics to diagnostic visualization and enable quantitative array selection without relying on external navigation sensors.

Across 54 scenarios (3 arrays × 6 DoFs × 3 imaging states), the hemispherical array consistently outperforms the planar and cubic layouts in both sidelobe metrics and PSI-based robustness ranking. Under the updated first-order non-ideality sensitivity analysis, the hemispherical array remains the best-performing geometry in the corrected state, with updated corrected global means of $PSLR = -28.6\ dB$ and $ISLR = -25.0\ dB$ over all six DoFs. Relative to the planar array, this corresponds to an improvement of approximately 6.5 dB in PSLR and 5.6 dB in ISLR. Relative to the cubic array, the hemispherical configuration retains an advantage of approximately 2.9 dB in PSLR and 2.9 dB in ISLR. These results confirm that the qualitative geometry ranking remains unchanged even after accounting for bounded first-order non-idealities.

For the individual motion components, the hemispherical array also preserves the strongest corrected sidelobe behavior. The largest hemisphere-over-planar corrected gain in PSLR occurs in Pitch, while the strongest ISLR advantage appears in Yaw. More broadly, the pairwise comparisons across Surge, Sway, Heave, Roll, Pitch, and Yaw show that three-dimensional apertures consistently reduce residual sidelobes after correction, with cubic generally ranking between the hemispherical and planar layouts. This indicates that distributing receiver baselines in three dimensions provides a persistent robustness benefit across both translational and rotational disturbances.

The PSI analysis clarifies the mechanism behind the hemispherical advantage. Distributing elements over a curved aperture with broad angular coverage lowers the effective rotational sensitivity and limits coherent accumulation of phase error along any single direction. The resulting reduction in normalized phase sensitivity is consistent with lower sidelobe levels and more stable main-lobe widths in the reconstructed images. Among the six motions, Yaw and Heave remain the most detrimental because they induce aperture-wide phase distortion and range-related modulation, whereas Roll is the least harmful for the geometries considered here. In these challenging cases, the hemispherical array shows the clearest advantage over planar layouts, in line with its lower effective PSI and improved sidelobe control.

The results provide clear operational guidance. When mission profiles imply elevated risk of rotational drift, heading variation, or vertical platform disturbance, the hemispherical array is the preferred choice, offering the best robustness per element among the tested geometries. Where curvature or packaging volume is constrained, a cubic layout still provides predictable mid-level improvements over a purely planar grid. In this sense, geometry-centric design should be viewed as complementary to autofocus and INS/DVL-based motion-compensation pipelines: improving the array geometry reduces the phase burden that downstream processing must correct.

The present study abstracts several aspects of the full operating environment, including reverberation, refraction, full multipath structure, mutual coupling, and manufacturing tolerances in the primary reconstruction loop. However, the added first-order sensitivity analysis indicates that these omitted non-idealities mainly shift the absolute values of PSI, PSLR, and ISLR, while preserving the qualitative ranking of the tested geometries under realistic perturbation budgets. The updated corrected global penalties remain moderate, and the hemispherical array continues to deliver the strongest overall sidelobe behavior within the motion-controlled framework adopted here.

Compared with representative prior multireceiver SAS methods reported in the literature, the proposed hemispherical configuration also maintains a substantially deeper corrected sidelobe floor. Using the updated corrected global means, it yields an approximately 13.1 dB deeper PSLR level and 13.5 dB deeper ISLR level relative to the average of the three reference methods considered. This indicates that starting from an optimized hydrophone geometry not only complements existing motion-compensation and autofocus techniques, but can also deliver materially better operational image quality.

Overall, by making motion sensitivity measurable through PSI and linking that sensitivity directly to

PSLR/ISLR and BP-consistent image interpretation, this study shows that hemispherical receiver arrays offer the most robust average performance under 6-DOF motion among the tested configurations. The results support the use of three-dimensional, near-isotropic hydrophone layouts as a practical design strategy for improving SAS robustness in embedded AUV platforms, especially when external navigation support is limited or residual motion errors cannot be fully eliminated.

7. Future Work

We outline a roadmap to turn the proposed geometry-centric approach into a field-ready capability, with emphasis on physics fidelity, PSI-aware design automation, and operational validation.

(1) Full-physics back-projection with measured trajectories. Replace the simplified visualization engine with end-to-end BP that ingests measured 6-DoF time histories.

(2) Motion spectra and analytical sensitivity. Extend beyond RMS magnitudes to spectral characterizations (colored noise; swell-induced narrowband components; control-loop transients). Derive closed-form PSI contributions for canonical spectra and correlate them with PSLR/ISLR trends. Deliverables: sensitivity charts for mission planners that map DoF, spectrum, and speed to expected sidelobe penalties.

(3) PSI-aware co-optimization of geometry and apodization. Formulate array design as multi-objective optimization: minimize normalized PSI and expected PSLR/ISLR while constraining volume, mass, wiring, and manufacturability. Variables include element locations (continuous on surfaces like hemispheres or discrete lattices), radius R, spacing d, and taper (Kaiser/Taylor). Explore sparse/irregular layouts for weight and cost reduction.

(4) Expanded modalities: bistatic/multistatic and heterogeneous arrays. Generalize the framework to separated Tx/Rx and mixed-aperture systems, where PSI has transmitted and receive components. Investigate whether hemispherical benefits persist when only the receiver is hemispherical, or when a hybrid (e.g., shallow dome + ring) is used.

(5) The present work deliberately uses single-DoF excitations to obtain interpretable, geometry-dependent sensitivities. A natural extension is to move to fully coupled 6-DoF trajectories, so that PSI and the proposed geometry ranking can be validated under realistic composite motions. Such experiments, using either high-fidelity simulators or measured AUV tracks, will clarify how well the hemispherical advantage persists when all motion components act simultaneously.

8. Acknowledgment

The authors gratefully acknowledge the SAR Research Center Laboratory and the Digital Signal Processing Laboratory, Faculty of Engineering, Ferdowsi University of Mashhad, for their support of this research and for providing the research facilities.

9. Symbols

B	LFM bandwidth [Hz]
c	Speed of sound in water [m/s]
d	Inter-element spacing of the array [m]
f_s	Sampling rate [Hz]
f_c	Center (carrier) frequency [Hz]
I(x)	1-D intensity profile used for PSLR/ISLR
N_{ping}	Number of pings in the synthetic aperture
R	Hemisphere radius array [m]
R_x, R_z, R_z	Rotation matrices about x, y, z axes
r_{body}	Hydrophone position in the body frame [m]
$r_{inertial}(t)$	Hydrophone position in the inertial frame [m]
$R_r(t)$	Receiver position at time t [m]
r_t	Target position [m]
s	Transmitter (Source) position [m]
T_P	Pulse length (LFM duration) [s]
$\hat{u}$	Unit look vector (receiver→target)
Δx	Along-track ping spacing [m]
θ	Pitch angle [rad]
ϕ	Roll angle [rad]

10. References

1- Zeng, S., Fan, W. and Du, X., (2022), *Three-Dimensional Imaging of Circular-Array Synthetic Aperture Sonar for Unmanned Surface Vehicle*, Sensors, Vol.22(10), p.3797. DOI: 10.3390/s22103797.

2- Gill, J. and Rama Rao, V.V.S., (2014), *Motion Compensation of Airborne Synthetic Aperture Radar*, IFAC Proceedings Volumes (Proc. 19th IFAC World Congress). DOI: 10.3182/20140313-3-IN-3024.00065.

3- Zhang, J., Cheng, G., Tang, J., Wu, H. and Tian, Z., (2023), *A Subaperture Motion Compensation Algorithm for Wide-Beam, Multiple-Receiver SAS Systems*, Journal of Marine Science and Engineering, Vol.11(8), p.1627. DOI: 10.3390/jmse11081627.

4- Zhang, X., Huang, P., Sun, H., Ying, W. and Yang, P., (2022), *Wide-Bandwidth Signal-Based Multireceiver SAS Imagery Using Extended Chirp Scaling Algorithm*, IET Radar, Sonar & Navigation, Vol.16(3), p.531–541. DOI: 10.1049/rsn2.12200.

5- Zhang, X., Yang, P. and Zhou, M., (2023), *Multireceiver SAS Imagery with Generalized PCA*, IEEE Geoscience and Remote Sensing Letters, Vol.20, p.1–5 (Art. 1502205). DOI: 10.1109/LGRS.2023.3286180.

6- Baron, V., Finez, A., Bouley, S., Fayet, F., Mars, J.I. and Nicolas, B., (2021), *Hydrophone Array Optimization, Conception, and Validation for Localization of Acoustic Sources in Deep-Sea Mining*, IEEE Journal of Oceanic Engineering, Vol.46(2), p.555–563. DOI: 10.1109/JOE.2020.3004018.

7- Król, J. and Błażejewski, A., (2020), *Fibonacci Array-Based Focused Acoustic Camera for Broad-Band Beamforming*, Journal of Sound and Vibration, Vol.478, p.115351. DOI: 10.1016/j.jsv.2020.115351.

8- Zhang, L., Liu, H., Liu, Y., et al., (2019), *Direction-of-Arrival Estimation with Structured Array Designs*, IET Microwaves, Antennas & Propagation. DOI: 10.1049/iet-map.2019.0518.

9- de Bree, H.E., Druyvesteyn, W.F. and co-authors, (2008), *Moving Microphone Arrays to Reduce Spatial Aliasing in the Beamforming Technique: Theoretical Background and Numerical Investigation*, Journal of the Acoustical Society of America, Vol.124(6), p.3648–3658. DOI: 10.1121/1.2998778.

10- Zhong, H., Zhou, Z., Zhang, P., et al., (2022), *An Efficient Multireceiver SAS Imaging Algorithm for Large Data in Heterogeneous Environment*, Research Square, Preprint. DOI: 10.21203/rs.3.rs-1624407/v.